Rayleigh wave H/V amplitude ratio measurement using multicomponent ambient noise cross-correlations, and its relationship to Vp/Vs

Authors : Ajay Malkoti[1],
Arjun Datta[1*],
Shravan M. Hanasoge[1]

Email : *arjun.datta@tifr.res.in

Affiliation: : [1]Department of Astronomy and Astrophysics,
Tata Institute of Fundamental Research
Homi Bhabha Road, Colaba, Mumbai 400005, India.

Abstract

The promise of passive seismology has increasingly been realized in recent years. Given the expense in installing and maintaining these seismic networks, it is important to extract as much information from the measurements as possible. In this context, the ellipticity or H/V amplitude ratio of Rayleigh waves can prove to be a valuable observable in ambient noise seismology due to its potential for constraining V_P structure, an advantage over group and phase-velocity dispersion, which are primarily sensitive to V_S. However, the suitability of the Rayleigh H/V ratio in noise-based studies depends on the accurate interpretation of measurements made on multi-component ambient-noise cross-correlations. We present a synthetic study that critically examines such measurements – commonly interpreted in terms of the Rayleigh H/V ratio – for realistic scenarios of spatially distributed and non-uniform noise sources. Using the Rayleigh-wave Green's function in a laterally homogeneous medium, we rigorously model multi-component cross-correlation for arbitrary noise-source distributions and extract from them standard estimates of the H/V ratio. Variation of these measurements with V_P is studied empirically by brute-force simulation. We find that the measurements depart significantly from the theoretical Rayleigh wave H/V for the medium in

question, when noise sources are strongly directional or anisotropic. However, the sensitivity to V_P structure is comparable to that of the classic Rayleigh wave H/V. We also propose a new measurement for cross-correlations that has slightly greater sensitivity to V_P. Finally, uncertainty analysis on synthetic tests suggests that the ellipticity measurements can robustly resolve the V_p structure in the presence of noise (up to 10%). The primary utility of this method in scenarios when the noise level in the measured cross-correlations is significant ($\gtrsim 20\%$), is in being able to discern between different classes of models.

Keywords: *Ambient noise; Cross-correlations; H/V ratio; Rayleigh waves;*

1 Introduction

Ambient noise cross-correlation is a popular technique used to study shallow Earth structure using observations of the ambient seismic field on Earth, commonly known as 'ambient noise'. The widespread use of this technique over the last 15 years has been largely based on the theoretical principle that the cross-correlation of a diffuse and equipartitioned noise wavefield recorded at two receivers, is proportional to the causal and anticausal far-field Green's function between them (Shapiro and Campillo, 2004; Snieder, 2004; Weaver and Lobkis, 2004). Heavy pre-processing of raw noise records and averaging of cross-correlations over sufficiently long times is adopted in practice (Bensen et al., 2007), to recover 'empirical Green's functions'. Even so, most applications recover only the surface-wave Green's function because the global noise field is dominated by ocean microseisms (Ardhuin et al., 2011, 2015) which originate near the Earth's surface and strongly excite seismic surface waves. Since the traditional surface-wave measurements of phase and group velocity dispersion are dominantly sensitive to shear-wave velocity (V_S), ambient noise has primarily been used to study Earth's V_S structure.

By contrast, recovery of P-wave velocities (V_P) from ambient noise is more challenging. Body waves, including P-waves, are hard to detect in ambient noise cross-correlations (due to weak excitation by shallow sources producing the noise wavefield) and the number of studies that have succeeded in doing so are limited (e.g. Roux et al., 2005a; Poli et al., 2012; Nakata et al., 2015, 2016; Liu et al., 2016; Saygin et al., 2017; Pedersen and Colombi, 2018; Wang et al., 2018). An alternative approach for studying V_P, that does not require P-wave observations, is to make use of the Rayleigh wave ellipticity or H/V ratio.

Rayleigh wave H/V ratio (ratio of horizontal to vertical component amplitudes) is an unconventional surface-wave observable that has a different sensitivity to Earth structure than the more widely used dispersion measurement. It has a shallower sensitivity to the three commonly used elastic parameters (V_P, V_S and density ρ; Tanimoto and Rivera,

2008; Muir and Tsai, 2017) and has been used in inversions to constrain ρ and V_p (Lin et al., 2012, 2014). Historically, the Rayleigh H/V ratio has seen limited use as a seismological imaging tool, perhaps due to the difficulty in obtaining stable measurements (Ferreira and Woodhouse, 2007; Tanimoto and Rivera, 2008). However, this has changed in recent years, with many researchers exploring its potential for probing upper-crustal structure, both in the context of classical earthquake seismology (Berbellini et al., 2016; Lin et al., 2012; Ringler et al., 2019; Yano et al., 2009) and noise tomography (Lin et al., 2014; Muir and Tsai, 2017). In the latter case, horizontal-to-vertical amplitude ratios obtained from multi-component cross-correlations are interpreted as the Rayleigh-wave H/V ratio, because the correlation signals are identified as containing Rayleigh waves (their presence established by observations of elliptical particle motion) travelling between pairs of stations. By way of disambiguation, we note that such measurements differ from the 'H/V spectral ratio' obtained from single-station noise records (Nakamura, 1989; Fäh et al., 2001) which may or may not be related to the Rayleigh wave H/V ratio (Bonnefoy-Claudet et al., 2006). In this paper, we are concerned only with the Rayleigh-wave H/V ratio.

With the maturing of the field of ambient-noise seismology, it is important to rigorously analyse the estimation of Rayleigh H/V ratios from seismic-noise data. The theoretical conditions for Green's-function retrieval from noise correlations are often not satisfied in reality due to non-stationary and heterogeneously distributed noise sources (Stehly et al., 2006; Ardhuin et al., 2011, 2015; Ermert et al., 2017). Consequently, a significant number of studies have warned of inaccurate empirical Green's functions that suffer from artefacts, as well as traveltime and amplitude errors (Fichtner, 2014; Froment et al., 2010; Halliday and Curtis, 2008; Kimman and Trampert, 2010; Tsai, 2009, 2011; Yao and van der Hilst, 2009). It is therefore to be expected that Rayleigh wave H/V ratios, which depend on relative amplitudes between components, are also similarly affected. The work of Xu and Mikesell (2017) explicitly confirms biases in the noise-correlation-derived Rayleigh-wave Green's tensor arising from heterogeneous noise sources.

In this study we do not invoke Green's function interpretations for noise-correlation signals; instead we model these signals rigorously for arbitrary spatial distributions of noise sources (Section 2). To our knowledge, no previous study that models cross-correlations in this manner has analysed the Rayleigh H/V measurement in detail. Through a series of synthetic tests, we quantify the dependence of this measurement on the anisotropy of noise-source distribution, as well as on model V_P, to assess its utility in practice (Sections 3 and 4). Measurement uncertainties, estimated by adding Gaussian

noise to synthetic cross-correlation waveforms, shed light on the resolving power with respect to V_P.

2 Methodology

2.1 Modelling theory

In this section, we describe how the multi-component CCs are synthesized and used to obtain measurements of H/V ratio. In the frequency domain, ensemble-averaged CCs under the assumption of spatially uncorrelated noise sources (Tromp et al., 2010; Sager et al., 2018; Fichtner and Tsai, 2019) take the general form:

$$\mathcal{C}_{pq}(\mathbf{x}_\alpha, \mathbf{x}_\beta) = \int_\oplus d\xi \; G^*_{pi}(\mathbf{x}_\alpha, \xi) G_{qj}(\mathbf{x}_\beta, \xi) S_{ij}(\xi) \tag{1}$$

where $\mathbf{x}_\alpha, \mathbf{x}_\beta$ are the receiver locations; G_{mn} are elements of the Green's tensor satisfying $\mathcal{L}G_{mn}(\mathbf{x}, \xi) = \delta_{mn}\delta(\mathbf{x}-\xi)$ for a wave operator $\mathcal{L}$ (subscripts m and n correspond to the component of motion at the receiver location $\mathbf{x}$ and the direction of the point force at the source location ξ, respectively); S_{ij} is the power spectral density (PSD) matrix of the noise sources, and the integral is over the Earth volume $\oplus$. In this study we simplify eq. (1) with a few assumptions. First, noise sources are assumed to be present only on the Earth's surface (e.g. Tromp et al., 2010), so the volume integral reduces to a surface integral over its upper boundary Ω, and we can restrict our modelling to just the surface-wave part of Green's function. Next, we consider noise sources acting in the vertical (z) direction only, so the PSD matrix reduces to a single term, i.e. $S_{ij} = S\delta_{ij}\delta_{i3}$. This ensures that we focus exclusively on Rayleigh waves, ignoring Love wave contributions in G. We further assume that the PSD is spatially uniform (Hanasoge, 2013, 2014; Datta et al., 2019) so that the spatial and frequency dependence of S may be separated, i.e. we write $S(\xi, \omega) = P(\omega)\sigma(\xi)$. These three simplifications lead to the expression:

$$\mathcal{C}_{pq}(\mathbf{x}_\alpha, \mathbf{x}_\beta; \omega) = P(\omega) \int_\Omega d\xi \; G^*_{pz}(\mathbf{x}_\alpha, \xi, \omega) G_{qz}(\mathbf{x}_\beta, \xi, \omega) \sigma(\mathbf{x}) \tag{2}$$

The evaluation of eq. (2) is still a three-step process in general, based on the invocation of source-receiver reciprocity at one of the receiver locations (Tromp et al., 2010; Sager et al., 2018). However in the specific case of working with a single receiver pair, as in this synthetic study, it is most efficient to invoke reciprocity at both receiver locations (Hanasoge, 2014; Xu et al., 2019), thereby rewriting eq. (2) as

$$\mathcal{C}_{pq}\left(\mathbf{x}_\alpha, \mathbf{x}_\beta, \omega\right) = \int_\Omega d\xi \; G^*_{zp}(\xi, \mathbf{x}_\alpha, \omega) \; G_{zq}(\xi, \mathbf{x}_\beta, \omega) \; P(\omega) \; \sigma(\mathbf{x}) \tag{3}$$

Hence $\mathcal{C}_{pq}$ is computed as follows. First, we obtain the z-component of impulse response in the entire horizontal domain for sources placed at the receiver locations and acting in the p and q directions. Next, we spatially integrate the product of the two responses (after complex conjugating one of them), weighted by the source mask σ.

This formulation is completely general with regard to the type of Earth model considered and the manner in which the Green's functions are obtained (e.g. analytically or numerically). In our implementation, we work with 1-D, vertically stratified media for which surface-wave terms of the elastodynamic Green's tensor are semi-analytically computable in 2-D as well as 3-D.

2.2 Computation of the Green's function

In our forward modelling scheme, we only need the Rayleigh-wave terms of Green's function in 3-D (point sources). For laterally homogeneous media, these are (Aki and Richards, 2002, Sec 7.4):

$$G \quad = \quad \sum_n \frac{1}{8cUI_1} \begin{bmatrix} r_1(h)r_1(z)\frac{x^2}{r^2} & r_1(h)r_1(z)\frac{xy}{r^2} & -ir_2(h)r_1(z)\frac{x}{r} \\ r_1(h)r_1(z)\frac{xy}{r^2} & r_1(h)r_1(z)\frac{y^2}{r^2} & -ir_2(h)r_1(z)\frac{y}{r} \\ ir_1(h)r_2(z)\frac{x}{r} & ir_1(h)r_2(z)\frac{y}{r} & r_2(h)r_2(z) \end{bmatrix} \times H_0^{(1)}(k_n r) \tag{4}$$

where all symbols follow the Aki and Richards (2002) notation and $r = \sqrt{x^2 + y^2}$. The expression in eq. (4) differs from the one in Aki and Richards (2002) in its use of Cartesian rather than cylindrical coordinates (we work with a Cartesian grid ξ), and in its abandonment of the far-field approximation — the Hankel function of the fist kind, $H_0^{(1)}$, is used instead of its asymptotic form, because the implementation of eq. (3) necessitates computation of Green's function at distances comparable to or shorter than the wavelength (see Sec 3.1).

To compute eq. (4), we solve the Rayleigh-wave eigenvalue problem by the method of Gomberg and Masters (1988), as in Datta et al. (2017); Datta (2018). This gives c, U and the displacement eigenfunctions r_1, r_2, which are numerically integrated to obtain I_1. Finally, we restrict our analysis to the fundamental mode ($n = 0$), and because we only need to evaluate G for sources and receivers on the surface, we use $h = z = 0$ in eq. (4).

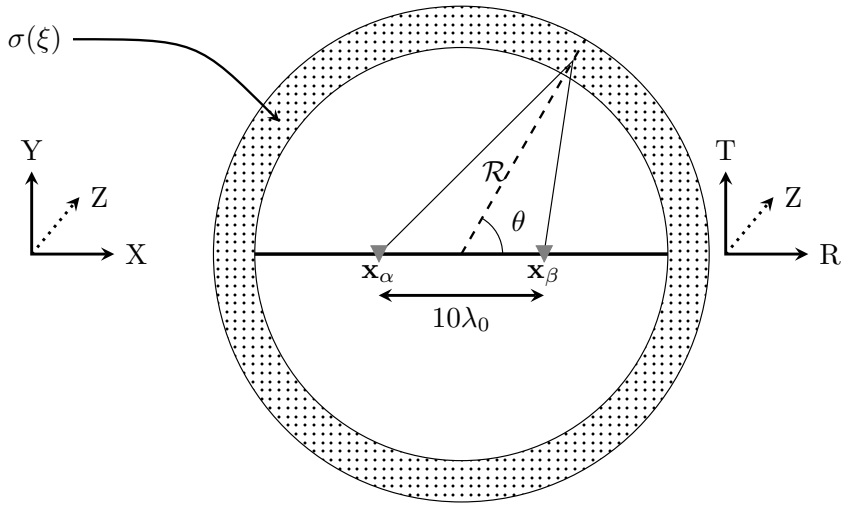

Figure 1: Schematic showing arrangement of sources (dots) and receivers (inverted triangles) in the modelling domain Ω. The coordinate axes R, T and Z, represent the radial, transverse and vertical directions respectively, for the receiver pair.

2.3 H/V ratio measurement

Rayleigh waves are polarized in the radial-vertical (R-Z) plane and their H/V ratio refers to the ratio η of the radial to vertical displacement amplitudes (e.g. Maupin, 2017). In a laterally homogeneous medium, η is easily obtained from the displacement eigenfunctions evaluated at the surface. By definition,

$$\eta(\omega) = \frac{r_1(z=0,\omega)}{r_2(z=0,\omega)}. \tag{5}$$

Equivalently, one may write

$$\eta = \frac{|G_{RZ}|}{|G_{ZZ}|} = \frac{|G_{RR}|}{|G_{ZR}|}. \tag{6}$$

The equivalence between eqs.(6) and (5) is seen from eq. (4), when the x, y axes are oriented along the radial and transverse directions respectively (e.g. Fig. 1). Since the second index in the Green's tensor G_{ij} refers to the source orientation, eq. (6) asserts that η is a medium property, independent of whether the source (point-force) is vertical or radial.

In the case of CCs, most studies define the Rayleigh H/V ratio analogously to eq. (6) using the corresponding elements of the cross-correlation tensor: $\mathcal{C}_{RR}, \mathcal{C}_{ZZ}, \mathcal{C}_{ZR}, \mathcal{C}_{RZ}$ (Lin et al., 2014; Muir and Tsai, 2017). If equivalence between cross-correlations and Green's function holds, the two CC measurements, Γ^R and Γ^Z, correspond to virtual sources oriented radially and vertically, respectively:

$$\Gamma^R = \frac{f(\mathcal{C}_{RR})}{f(\mathcal{C}_{ZR})} \sim \eta$$
$$\Gamma^Z = \frac{f(\mathcal{C}_{RZ})}{f(\mathcal{C}_{ZZ})} \sim \eta. \tag{7}$$

Here, f represents the operations applied to the CCs to obtain robust measurements. In this study, we 1) Determine the envelope of the cross-correlation signal, 2) Pick its maximum value on the causal and anti-causal branches, 3) Average the two values thus obtained.

We note that the interpretation of Γ^R or Γ^Z as the Rayleigh wave H/V ratio (right side of eq. (7)) is supported in this study by the fact that the CCs are constructed from Rayleigh waves alone. The superscript of these ratios in eq. (7) represents the virtual source direction. On the other hand, since cross-correlations and Green's functions are not equivalent (e.g. Roux et al., 2005b), especially when source illumination is anisotropic, we define a third measurement Γ, which does not afford an interpretation in terms of a virtual source. The term Γ makes use of $\mathcal{C}_{RR}$ and $\mathcal{C}_{ZZ}$, and based on the forward model eq. (2), we estimate that it should be related to η^2:

$$\Gamma = \frac{f(\mathcal{C}_{RR})}{f(\mathcal{C}_{ZZ})} \sim \eta^2. \tag{8}$$

3 Simulations

We perform a suite of simulations designed to empirically assess the sensitivity of H/V measurements to V_p structure, as well as gross geometrical features of the noise-source distribution σ. These are the two quantities which we vary in our forward modelling, while other parameters are held fixed. As explained in the previous section, our modelling scheme entails a 1-D, depth-dependent Earth model $M(z)$ in which the Green's functions are computed, and a 2-D horizontal domain $\Omega(x, y)$ on which the sources are distributed (the Earth model is implicitly uniform throughout Ω). Here we first describe the fixed parameters, pertaining to Ω, and then the model variations, which involve both M and Ω.

3.1 Fixed parameters

Rayleigh wave H/V ratio is a frequency-dependent quantity but for the sake of simplicity, we present results in this paper for a single frequency, $f_0 = 0.1$ Hz. This value (10 s period) is chosen because it lies in between the primary and secondary microseism peaks

at $\sim$ 7 and 15 s. (Peterson, 1993; Ardhuin et al., 2015). This choice of frequency dictates nearly all other choices relating to the simulation geometry. We model the PSD of the noise sources, $P(\omega)$, with a narrow-band Gaussian centered at $f_0 = 0.1$ Hz (see Fig. 3f). The corresponding wavelength, λ_0, is used to fix the uniform grid spacing $\Delta h \leq \lambda_0/4$ and separation between receivers, $|\mathbf{x}_\alpha - \mathbf{x}_\beta| \geq 10\lambda_0$, well above the typical requirement of three wavelengths (Bensen et al., 2007; Luo et al., 2015). The size of the domain Ω is chosen to be at least twice the receiver separation in both directions, i.e., $[x_{min}, x_{max}, y_{min}, y_{max}] = 20\lambda_0 \times [-1, 1, -1, 1]$.

We have $\lambda_0 \approx 35$ km for Earth model M_0 (section 3.2), which leads to the values $\Delta h = 8$ km, $\mathbf{x}_\alpha = (-164 \text{ km}, 0)$, $\mathbf{x}_\beta = (164 \text{ km}, 0)$ and $\Omega = \{-600 \text{ km} < x < 600 \text{ km}, -600 \text{ km} < y < 600 \text{ km}\}$. Note that the receivers are kept off-grid, since they are turned into sources in our implementation eq. (3). Finally, we use a temporal sampling interval of 1 s and generate a time series of length 400 s.

3.2 Models used

The 1-D Earth model we work with is PREM (Dziewonski and Anderson, 1981) without the ocean layer; we call this model M_0. Simulations are performed for 20 variants of this model, which differ only in their V_p values — a relative perturbation in the range -9% to $+10\%$ is applied uniformly at all depths to the model V_p.

Each Earth model M is used in conjunction with a particular model for the source distribution σ over the domain Ω. We use different classes of σ. *Uniform distribution* where the sources have uniform strength everywhere in the domain; *Ring distribution* where sources are present at some distance ($\mathcal{R}$) from the center of domain within a strip of width $d\mathcal{R}$ (Fig. 1), and *Arc distribution* where sources are confined to an arc, with given $\mathcal{R}$ and $d\mathcal{R}$, oriented at some angle to the receiver pair. We use $\mathcal{R} = 250$ km and $d\mathcal{R} = 40$ km for ring and arc distributions. Three arc distributions are implemented to cover the range of possible scenarios of source directionality with respect to the receiver pair: *parallel* ($\theta = -15°$ to $15°$), *oblique* ($\theta = 30°$ to $60°$), and *orthogonal* ($\theta = 75°$ to $105°$). The arcs have uniform source strength in the aforementioned ranges for θ, but are cosine tapered to zero over an additional $5°$ at both ends.

The five source-distribution models utilized for the simulations are shown in Fig. 2.

4 Analysis and results

We start by examining the CC obtained for each of the noise-source distributions in Earth model M_0 (Fig. 3) . The effect of anisotropic source distributions is readily observed on the amplitude (in positive and negative branches, A^+, A^-) as well as arrival

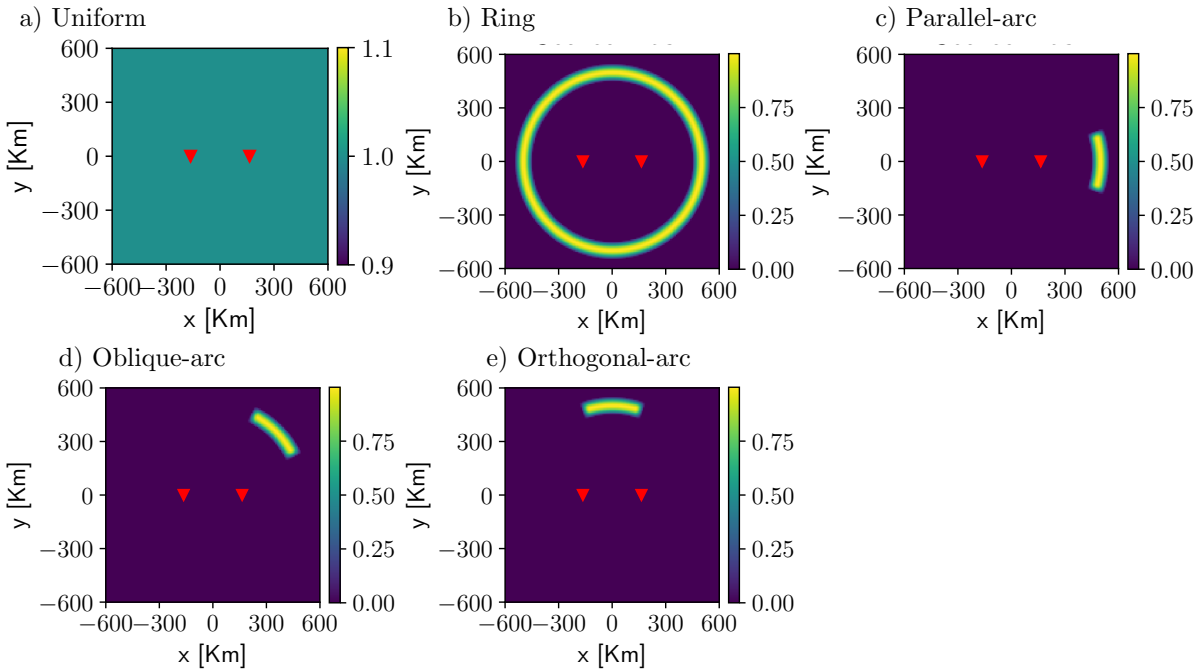

Figure 2: Different noise source distributions as defined in the text and identified here by the individual plot titles. The red triangles mark the receiver locations.

time (T_{CC}) of signals in the CC. Uniform and ring distributions show $A^+ = A^-$ and nearly the same arrival times as for Rayleigh waves (T_R) with one of the receivers acting as a virtual source. In contrast, the arc-type distributions have $A^+ \neq A^-$ and $T_{CC} = T_R$ holds only for the parallel-arc configuration. These observations are well understood in terms of stationary and non-stationary phase sources (e.g. Xu and Mikesell, 2017).

Next, we look at various H/V measurements obtained for all our Earth models with varying V_P. Fig. 4 shows that the H/V ratio measurements for the uniform and ring distributions have an excellent match with the theoretical Rayleigh wave H/V ratio, i.e. we find $\Gamma^R = \Gamma^Z \approx \eta$ and $\Gamma \approx \eta^2$. On the question of sensitivity to V_p, this implies that Γ offers better resolution than Γ^R or Γ^Z — the 'dynamic range' of η, i.e. the difference between its maximum and minimum values over the range of Earth models used, is $\eta_{DR} =\approx 0.085$ whereas for η^2 it is slightly higher, ${\eta^2}_{DR} \approx 0.104$ (also apparent from the slopes of the graphs in Fig. 4).

Moving on to the anisotropic (arc-type) noise source distributions, the condition $\Gamma^R = \Gamma^Z$ continues to hold in all cases, but the equivalence relations between the CC-derived H/V and the theoretical Rayleigh wave H/V, break down for the oblique-arc and orthogonal-arc distributions. The discrepancies are particularly large in the latter case, and are consistent over the range of Earth models used. A quantitative summary is provided in Table 1.

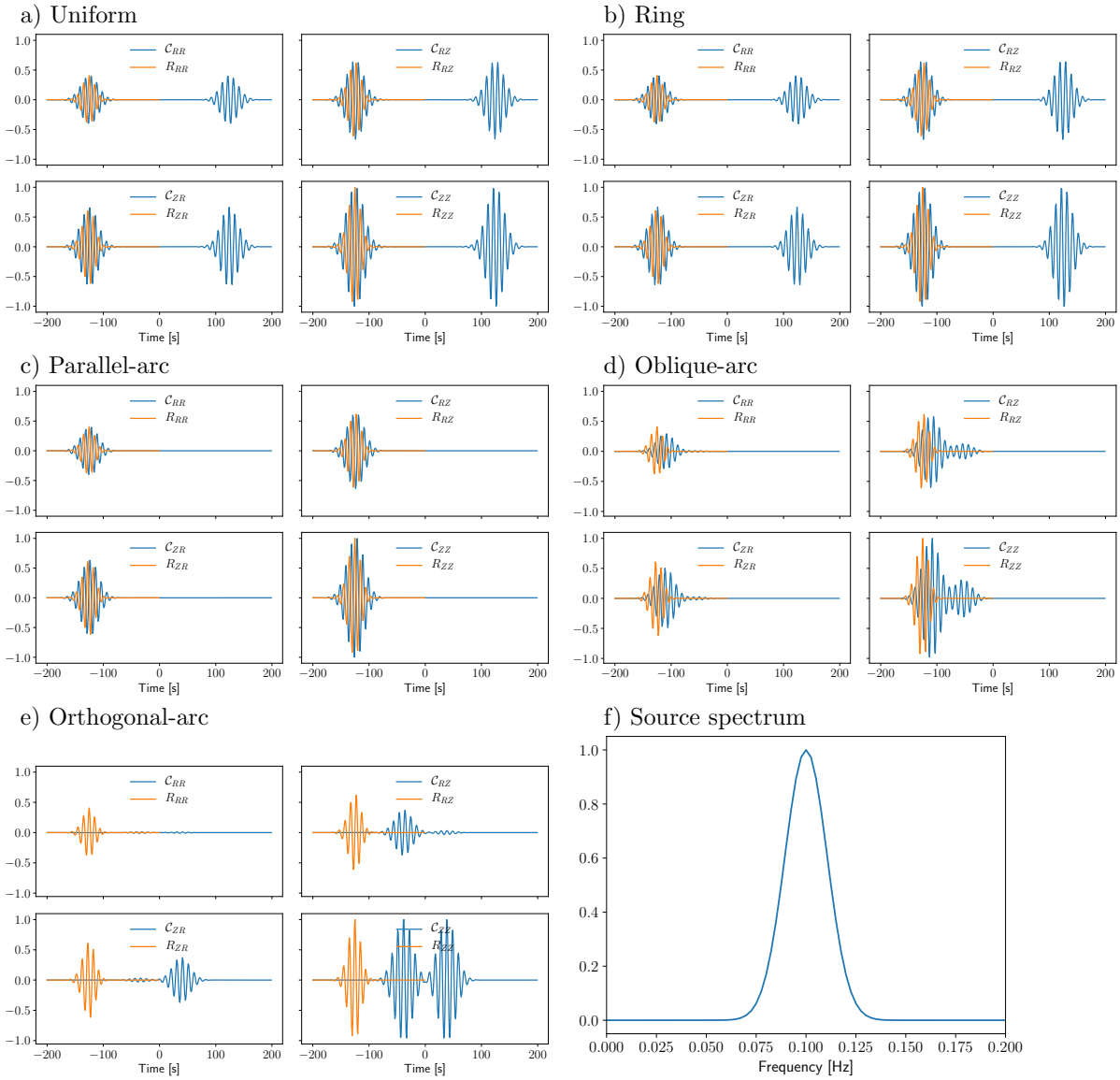

Figure 3: Panels (a)-(e) show the synthetic CCs generated for the corresponding source distributions in Fig. 2. Each panel contains four plots for the four components (clockwise from top left) $\mathcal{C}_{RR}$, $\mathcal{C}_{RZ}$, $\mathcal{C}_{ZZ}$ and $\mathcal{C}_{ZR}$. The corresponding Rayleigh wave from receiver α to receiver β has also been presented for comparison. The amplitudes are normalized with respect to the maximum within a panel. (f) $P(\omega)$ for the noise sources, centred at 0.1 Hz.

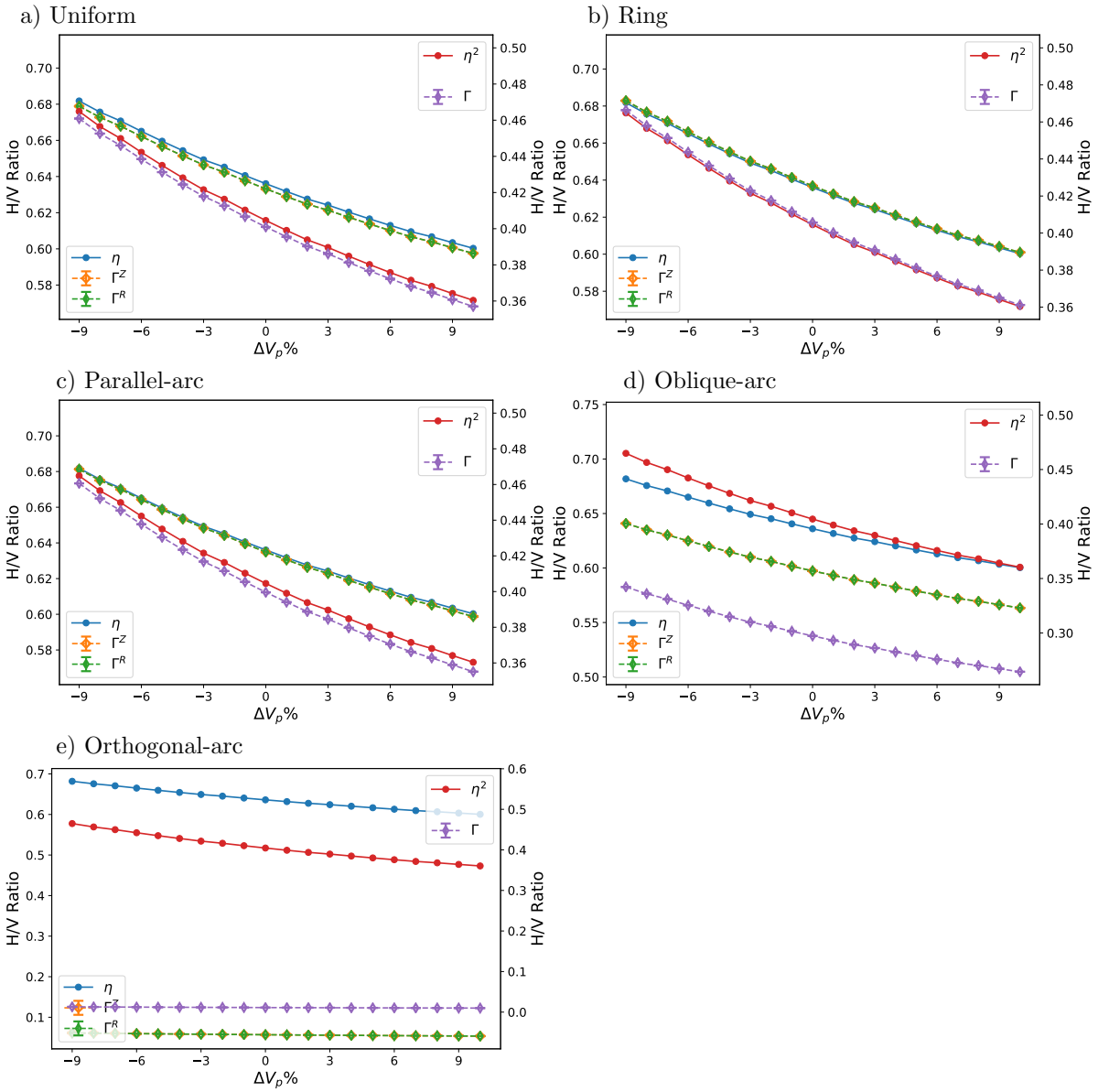

Figure 4: H/V ratio measurements obtained from CCs for different noise source distributions (as indicated in the plot titles a-e), and compared with the Rayleigh wave H/V for the medium, which is unrelated to noise source distribution. Note that we have used separate y-axes for different curves, shown on the left and right sides of each plot. The legend boxes attached to these two axes identify the curves associated.

4.1 Measurements with added synthetic noise

Since our aim in this study is to assess the sensitivity of H/V measurements to V_P, we compute uncertainty estimates for the measurements by adding noise to our CC waveforms. The magnitudes of uncertainties, compared with the dynamic range of the measurements (over the range of V_P values considered) sheds light on the usefulness of these measurements in practice. Synthetic waveforms with noise, $\tilde{S}(t)$ may be obtained by adding noise $N(t)$, of chosen strength, to the noise-free signal $S(t)$, as

$$\tilde{S}(t) = S(t) + \frac{\alpha\, k}{100}\, N(t), \tag{9}$$

where α is the desired signal to noise ratio and k is a scaling factor to bring the noise amplitudes to the signal level. N is computed in the frequency domain, using the power spectrum of the signal:

$$N(\omega) = P(\omega)\chi(\omega) \tag{10}$$

where $P(\omega) = S^*(\omega)S(\omega), \quad \chi(\omega) = [\mathcal{N}(0,1) + j\mathcal{N}(0,1)]/\sqrt{2}$ and $\mathcal{N}(\mu, s)$ represents a Gaussian random variable with mean, μ, and standard deviation, s.

H/V ratio calculations are performed for a given amount of noise (viz. 2%, 5% and 10%) and for each source distribution and Earth model, using all three H/V ratios eq. (7) and eq. (8). The results are shown in Fig. 5, with standard error estimated from 1000 realizations of added random noise.

As in the noise-free case, the mean trend of estimated H/V ratio in the presence of added noise closely follows the theoretical curves for homogeneous, ring and parallel-arc distributions. For the oblique-arc distribution there is a significant departure of mean trend from the theoretical curves containing a large error. For the orthogonal-arc distribution the H/V observation are completely erroneous. The uncertainty in estimated H/V ratios (Γ^R, Γ^Z, and Γ) in the presence of noise is presented in Table 1. This helps us evaluate the efficacy of measurements based on the thresholds given by η_{DR} for Γ^R and Γ^Z, and by ${\eta^2}_{DR}$ for Γ. We infer two things from the observed values. First, meaningful measurements can only be made for up to 15% random Gaussian noise. Beyond this noise level, the uncertainties in CC-derived H/V ratios exceed the η_{DR} or ${\eta^2}_{DR}$ thresholds. Second, noise has a lower impact on Γ in comparison to Γ^R and Γ^Z, due to its larger dynamic range.

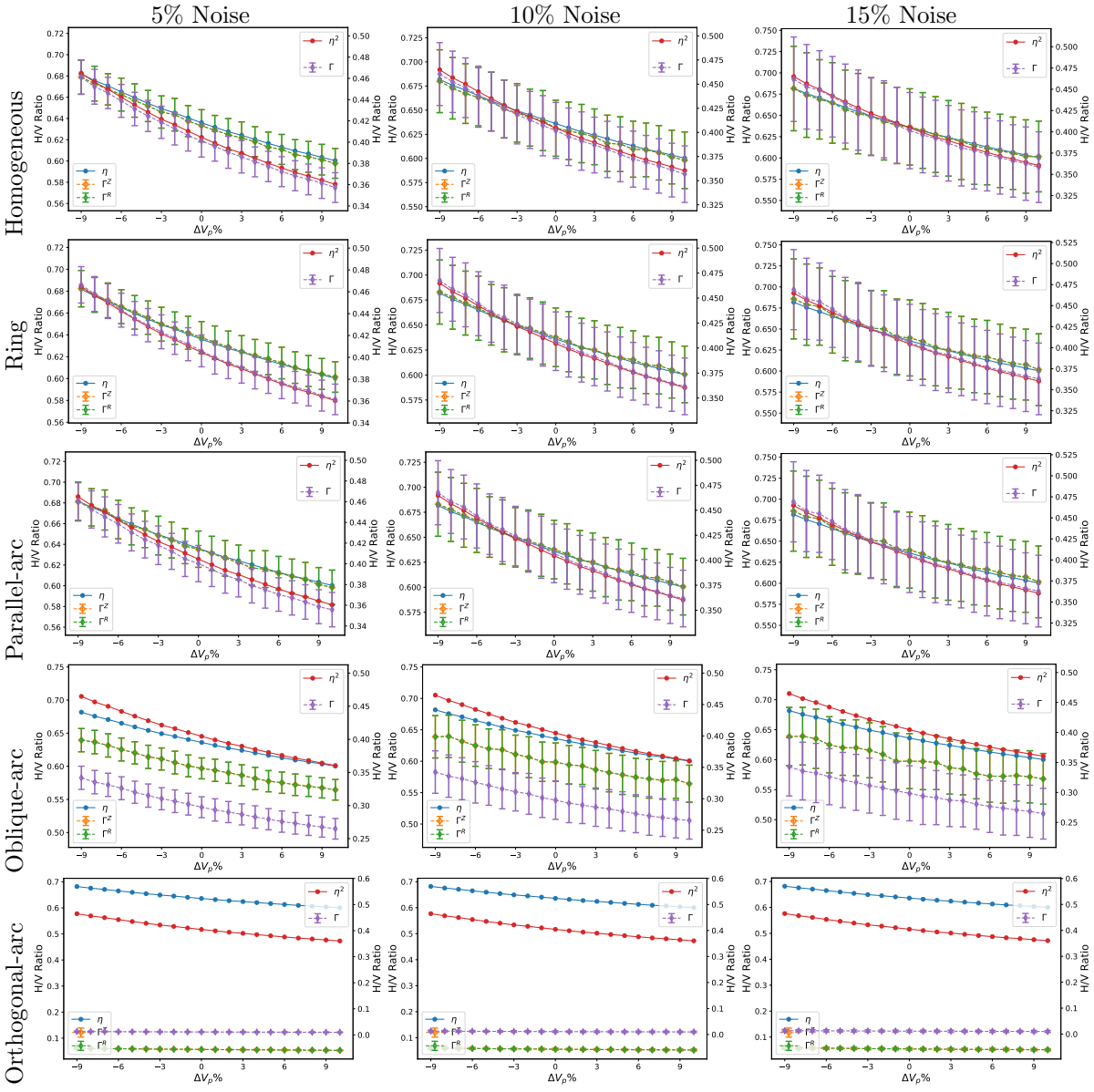

Figure 5: Similar to Fig. 4 but for measurements made with synthetic noise added to the CC. Noise levels vary across columns as indicated in the top panel, and rows correspond to source distributions as indicated on the extreme left.

Noise %		**Uniform**	**Ring**	**Parallel-arc** ($-30°$ to $30°$)	**Oblique-arc** ($15°$ to $75°$)	**Orthogonal-arc** ($60°$ to $120°$)
0%	$A^+ = A^-$	$\surd$	$\surd$	$\times$	$\times$	$\times$
0%	$T_R = T_{CC}$	$\surd$	$\surd$	$\surd$	$\surd$	$\times$
0%	$\eta - \Gamma^Z$	0.4%	0.2%	0.2%	61%	91%
0%	$\eta - \Gamma^R$	0.4%	0.2%	0.2%	61%	91%
0%	$\eta^2 - \Gamma$	0.8%	0.4%	1.2%	26%	97%
	Range of estimated H/V (Threshold $\Delta\eta_{DR} = 0.085$, $\Delta\eta^2_{DR} = 0.104$)					
2%	$\Delta\Gamma^Z = \Delta\Gamma^R$	0.012 $\downarrow$	0.012 $\downarrow$	0.014 $\downarrow$	0.013 $\downarrow$	NA
	$\Delta\Gamma$	0.008 $\downarrow$	0.008 $\downarrow$	0.009 $\downarrow$	0.007 $\downarrow$	NA
5%	$\Delta\Gamma^Z = \Delta\Gamma^R$	0.030 $\downarrow$	0.030 $\downarrow$	0.035 $\downarrow$	0.033 $\downarrow$	NA
	$\Delta\Gamma$	0.019 $\downarrow$	0.019 $\downarrow$	0.022 $\downarrow$	0.016 $\downarrow$	NA
10%	$\Delta\Gamma^Z = \Delta\Gamma^R$	0.060 $\downarrow$	0.060 $\downarrow$	0.067 $\downarrow$	0.063 $\downarrow$	NA
	$\Delta\Gamma$	0.037 $\downarrow$	0.038 $\downarrow$	0.042 $\downarrow$	0.031 $\downarrow$	NA
15%	$\Delta\Gamma^Z = \Delta\Gamma^R$	0.090 $\sim$	0.090 $\sim$	0.096 $\uparrow$	0.091 $\sim$	NA
	$\Delta\Gamma$	0.057 $\downarrow$	0.058 $\downarrow$	0.061 $\downarrow$	0.045 $\downarrow$	NA

Table 1: A tabular representation of results. First row shows whether the amplitude on positive and negative branch are equal. Second row show if the rayleigh wave travel time matches with waveform in CC. Third to fifth row shows the difference between the theoretical H/V ratio for Rayleigh wave and the one calculated using CC. Rest of the rows below represent measurement uncertainties, i.e. the size of error bars, estimated with added random noise. Up/down-arrows represent higher/lower values than the theoretical dynamic range threshold and $\sim$ represents close to the threshold.

5 Discussion and conclusions

We have presented a synthetic study that critically examines measurements commonly used to estimate the Rayleigh-wave ellipticity or H/V amplitude ratio from multi-component CCs. The study focuses on two aspects of these measurements: the extent to which they are degraded on account of anisotropic distributions of ambient noise sources, and their variations with model V_P. Both aspects are analysed empirically, by modelling cross-correlations for some simple distributions of noise sources, and a suite of 1-D Earth models that differ in V_P. Our results demonstrate that the absolute values of CC-based H/V measurements are adversely affected by strongly anisotropic noise sources (off the receiver line), and that the sensitivity to V_P can be marginally enhanced by taking the ratio of the $\mathcal{C}_{RR}$ and $\mathcal{C}_{ZZ}$ components of the cross-correlation tensor. This measurement, Γ, defies conventional Green's function interpretations for cross-correlations because it cannot be associated with a common virtual source. It however recovers the square of the Rayleigh H/V ratio when noise sources are not strongly anisotropic. Finally, uncertainty analysis reveals that V_p structure may be resolved in the presence of noise in the correlation measurements (up to 10%).

It should be borne in mind that our results are qualified by the modelling assumptions

we have used (Section 2). For example, because we assume only vertically directed sources, we have excluded Love-wave contributions in our analysis. In general, Love waves from laterally (horizontally) directed noise sources will additionally contribute to the radial-component displacement, impacting the corresponding cross-correlations and therefore the H/V-ratio measurements. However, this requires reliably determining the true orientations of noise sources (i.e. horizontal or vertical and their directionality with respect to the network), a challenging problem; we defer these modelling tasks to a future effort.

Acknowledgement

This work was funded by Shell India Markets Pvt.Ltd. A.D. acknowledges support from Shell contract PT75508.

References

Aki, K. and Richards, P. G. (2002). *Quantitative seismology*. University Science Books.

Ardhuin, F., Gualtieri, L., and Stutzmann, E. (2015). How ocean waves rock the Earth: Two mechanisms explain microseisms with periods 3 to 300 s. *Geophys. Res. Lett.*, 42(3):765–772.

Ardhuin, F., Stutzmann, E., Schimmel, M., and Mangeney, A. (2011). Ocean wave sources of seismic noise. *J. Geophys. Res.*, 116(C9):C09004.

Bensen, G. D., Ritzwoller, M. H., Barmin, M. P., Levshin, A. L., Lin, F., Moschetti, M. P., Shapiro, N. M., and Yang, Y. (2007). Processing seismic ambient noise data to obtain reliable broad-band surface wave dispersion measurements. *Geophys. J. Int.*, 169(3):1239–1260.

Berbellini, A., Morelli, A., and Ferreira, A. M. G. (2016). Ellipticity of Rayleigh waves in basin and hard-rock sites in Northern Italy. *Geophys. J. Int.*, 206(1):395–407.

Bonnefoy-Claudet, S., Cornou, C., Bard, P. Y., Cotton, F., Moczo, P., Kristek, J., and Fäh, D. (2006). H/V ratio: A tool for site effects evaluation. Results from 1-D noise simulations. *Geophys. J. Int.*, 167(2):827–837.

Datta, A. (2018). SWRT: A package for semi-analytical solutions of surface wave propagation, including mode conversion, across transversely aligned vertical discontinuities. *Geosci. Instrum., Methods Data Syst.*, 75194:101–112.

Datta, A., Hanasoge, S., and Goudswaard, J. (2019). Finite frequency inversion of cross-correlation amplitudes for ambient noise source directivity estimation. *J. Geophys. Res.*, 124.

Datta, A., Priestley, K. F., Roecker, S., and Chapman, C. H. (2017). Surface wave mode coupling and the validity of the path average approximations in surface waveform inversions: an empirical assessment. *Geophys. J. Int.*, 211(2):1099–1120.

Dziewonski, A. M. and Anderson, D. L. (1981). Preliminary reference Earth model. *Phys. Earth Planet. Inter.*, 25(4):297–356.

Ermert, L., Sager, K., Afanasiev, M., Boehm, C., and Fichtner, A. (2017). Ambient Seismic Source Inversion in a Heterogeneous Earth: Theory and Application to the Earth's Hum. *J. Geophys. Res.*, 122(11):9184–9207.

Ferreira, A. M. G. and Woodhouse, J. H. (2007). Observations of long period Rayleigh wave ellipticity. *Geophys. J. Int.*, 169(1):161–169.

Fichtner, A. (2014). Source and processing effects on noise correlations. *Geophys. J. Int.*, 197(3):1527–1531.

Fichtner, A. and Tsai, V. C. (2019). Theoretical Foundations of Noise Interferometry. In Nakata, N., Gualtieri, L., and Fichtner, A., editors, *Seismic Ambient Noise*, pages 109–143. Cambridge University Press, 1 edition.

Froment, B., Campillo, M., Roux, P., Gouédard, P., Verdel, A., and Weaver, R. L. (2010). Estimation of the effect of nonisotropically distributed energy on the apparent arrival time in correlations. *Geophysics*, 75(5):SA85–SA93. Publisher: Society of Exploration Geophysicists.

Fäh, D., Kind, F., and Giardini, D. (2001). A theoretical investigation of average H/V ratios. *Geophys. J. Int.*, 145(2):535–549.

Gomberg, J. S. and Masters, T. G. (1988). Waveform modelling using locked-mode synthetic and differential seismograms: application to determination of the structure of Mexico. *Geophys. J. Int.*, 94(2):193–218.

Halliday, D. and Curtis, A. (2008). Seismic interferometry, surface waves and source distribution. *Geophys. J. Int.*, 175(3):1067–1087.

Hanasoge, S. M. (2013). The influence of noise sources on cross-correlation amplitudes. *Geophys. J. Int.*, 192(1):295–309.

317 Hanasoge, S. M. (2014). Measurements and kernels for source-structure inversions in
318 noise tomography. *Geophys. J. Int.*, 196:971–985.

319 Kimman, W. P. and Trampert, J. (2010). Approximations in seismic interferometry and
320 their effects on surface waves. *Geophys. J. Int.*, 182(1):461–476.

321 Lin, F.-C., Schmandt, B., and Tsai, V. C. (2012). Joint inversion of Rayleigh wave phase
322 velocity and ellipticity using USArray: Constraining velocity and density structure in
323 the upper crust. *Geophys. Res. Lett.*, 39(12):L12303.

324 Lin, F. C., Tsai, V. C., and Schmandt, B. (2014). 3-D crustal structure of the western
325 United States: Application of Rayleigh-wave ellipticity extracted from noise cross-
326 correlations. *Geophys. J. Int.*, 198(2):656–670.

327 Liu, Q., Koper, K. D., Burlacu, R., Ni, S., Wang, F., Zou, C., Wei, Y., Gal, M., and
328 Reading, A. M. (2016). Source locations of teleseismic P, SV, and SH waves observed in
329 microseisms recorded by a large aperture seismic array in China. *Earth and Planetary*
330 *Science Letters*.

331 Luo, Y., Yang, Y., Xu, Y., Xu, H., Zhao, K., and Wang, K. (2015). On the limitations of
332 interstation distances in ambient noise tomography. *Geophys. J. Int.*, 201(2):652–661.

333 Maupin, V. (2017). 3-D sensitivity kernels of the Rayleigh wave ellipticity. *Geophys. J.*
334 *Int.*, 211(1):107–119.

335 Muir, J. B. and Tsai, V. C. (2017). Rayleigh-Wave H/V via Noise Cross Correlation in
336 Southern California. *Bull. Seism. Soc. Am.*, 107(5):2021–2027.

337 Nakamura, Y. (1989). A method for dynamic characteristics estimation of subsurface
338 using microtremor on the ground surface. *Railway Technical Research Institute, Quar-*
339 *terly Reports*, 30(1).

340 Nakata, N., Boué, P., Brenguier, F., Roux, P., Ferrazzini, V., and Campillo, M. (2016).
341 Body and surface wave reconstruction from seismic noise correlations between arrays
342 at Piton de la Fournaise volcano. *Geophys. Res. Lett.*, 43(3):1047–1054.

343 Nakata, N., Chang, J. P., Lawrence, J. F., and Boué, P. (2015). Body wave extraction
344 and tomography at Long Beach, California, with ambient-noise interferometry. *J.*
345 *Geophys. Res.*, 120(2):1159–1173.

346 Pedersen, H. A. and Colombi, A. (2018). Body waves from a single source area observed
347 in noise correlations at arrival times of reflections from the 410 discontinuity. *Geophys.*
348 *J. Int.*

Peterson, J. R. (1993). Observations and modeling of seismic background noise. USGS Numbered Series 93-322, U.S. Geological Survey. Code Number: 93-322 Code: Observations and modeling of seismic background noise Publication Title: Observations and modeling of seismic background noise Reporter: Observations and modeling of seismic background noise Series: Open-File Report.

Poli, P., Pedersen, H. A., and Campillo, M. (2012). Emergence of body waves from cross-correlation of short period seismic noise. *Geophys. J. Int.*, 188(2):549–558.

Ringler, A. T., Wilson, D. C., Zürn, W., and Anthony, R. E. (2019). Rayleigh wave ellipticity measurement uncertainty across the IRIS/USGS and New China Digital Seismograph Networks. *Geophys. J. Int.*, 217(1):219–237.

Roux, P., Sabra, K. G., Gerstoft, P., Kuperman, W. A., and Fehler, M. C. (2005a). P-waves from cross-correlation of seismic noise. *Geophys. Res. Lett.*, 32(19):L19303.

Roux, P., Sabra, K. G., Kuperman, W. A., and Roux, A. (2005b). Ambient noise cross correlation in free space: Theoretical approach. *J. Acoust. Soc. Am.*, 117(1):79–84.

Sager, K., Ermert, L., Boehm, C., and Fichtner, A. (2018). Towards full waveform ambient noise inversion. *Geophys. J. Int.*, 212(1):566–590.

Saygin, E., Cummins, P. R., and Lumley, D. (2017). Retrieval of the P wave reflectivity response from autocorrelation of seismic noise: Jakarta Basin, Indonesia. *Geophys. Res. Lett.*, 44(2).

Shapiro, N. M. and Campillo, M. (2004). Emergence of broadband Rayleigh waves from correlations of the ambient seismic noise. *Geophys. Res. Lett.*, 31(7).

Snieder, R. (2004). Extracting the Green's function from the correlation of coda waves: A derivation based on stationary phase. *Phys. Rev. E*, 69(4):046610. Publisher: American Physical Society.

Stehly, L., Campillo, M., and Shapiro, N. M. (2006). A study of the seismic noise from its long-range correlation properties. *J. Geophys. Res.*, 111(B10):B10306.

Tanimoto, T. and Rivera, L. (2008). The ZH ratio method for long-period seismic data: sensitivity kernels and observational techniques. *Geophys. J. Int.*, 172(1):187–198.

Tromp, J., Luo, Y., Hanasoge, S., and Peter, D. (2010). Noise cross-correlation sensitivity kernels. *Geophys. J. Int.*, 183(2):791–819.

Tsai, V. C. (2009). On establishing the accuracy of noise tomography travel-time measurements in a realistic medium. *Geophys. J. Int.*, 178(3):1555–1564. Publisher: Oxford Academic.

Tsai, V. C. (2011). Understanding the amplitudes of noise correlation measurements. *J. Geophys. Res.*, 116(B9):B09311.

Wang, W., Gerstoft, P., and Wang, B. (2018). Seasonality of P wave microseisms from NCF-based beamforming using ChinArray. *Geophys. J. Int.*, 213(3):1832–1848.

Weaver, R. L. and Lobkis, O. I. (2004). Diffuse fields in open systems and the emergence of the Green's function (L). *J. Acoust. Soc. Am.*, 116(5):2731–2734. Publisher: Acoustical Society of America.

Xu, Z. and Mikesell, T. D. (2017). On the reliability of direct Rayleigh-wave estimation from multicomponent cross-correlations. *Geophys. J. Int.*, 210(3):1388–1393.

Xu, Z., Mikesell, T. D., Gribler, G., and Mordret, A. (2019). Rayleigh-wave multicomponent cross-correlation-based source strength distribution inversion. Part 1: Theory and numerical examples. *Geophys. J. Int.*, 218(3):1761–1780.

Yano, T., Tanimoto, T., and Rivera, L. (2009). The ZH ratio method for long-period seismic data: inversion for S-wave velocity structure. *Geophys. J. Int.*, 179(1):413–424.

Yao, H. and van der Hilst, R. D. (2009). Analysis of ambient noise energy distribution and phase velocity bias in ambient noise tomography, with application to SE Tibet. *Geophys. J. Int.*, 179(2):1113–1132.